Sensors and Actuators A 284 (2018) 158–167

Contents lists available at ScienceDirect

Sensors and Actuators A: Physical

journal homepage: www.elsevier.com/locate/sna

Ultrasonic motors with poly phenylene sulfide/alumina/PZT triple-layered vibrators

Jiang Wu*, Yosuke Mizuno, Kentaro Nakamura

Laboratory for Future Interdisciplinary Research of Science and Technology, Tokyo Institute of Technology, Yokohama 226-8503, Japan

ARTICLE INFO

Article history:
Received 28 July 2018
Received in revised form 8 September 2018
Accepted 26 September 2018
Available online 4 October 2018

Keywords:
Ultrasonic motors
Vibrators
Triple layer
Alumina
Poly phenylene sulfide

ABSTRACT

Our previously reported ultrasonic motors with poly phenylene sulfide (PPS)/lead zirconate titanate (PZT) double-layered vibrators were capable of providing high rotation speeds and light weight, but their output torques and power were limited owing to the low stiffness of PPS vibrating bodies. In this study, we constructed a triple-layered vibrator by sandwiching a thin alumina disk between the PPS vibrating body and PZT disk to compensate the stiffness. First, their fundamental vibration characteristics were investigated as some of key dimensions were varied. The force factor of the PPS/alumina/PZT triple-layered vibrator reached the maximal value when the neutral axis located at the boundary between the PZT and alumina disks. In contrast, the neutral axes existed in the PZT disks for the PPS/PZT double-layered vibrators; this caused the relatively low force factors compared to the triple-layered vibrators. Subsequently, the load characteristics of the PPS/alumina/PZT triple-layered motors were experimentally assessed. The maximum output torque and power of the triple-layered motors were 5 and 13 times the values of the double-layered motors, respectively, owing to the enhanced force factor and electromechanical coupling factor. Besides, the optimal thickness was lower for the triple- than for the double-layered motor. These advantages indicate the potential of our newly designed triple-layered motors for practical applications.

1. Introduction

Ultrasonic motors (USMs) exhibit high output torques at low rotational speeds [1,2], simple structures [3], and fast responses [4,5]. Currently, they have some special applications, e.g. auto-focus lenses in digital cameras or optical instruments [6,7]. Recently, USMs capable of working in acid or alkaline environments have become increasingly demanded as potential key actuators of robots for the chemical industry [8,9]. However, the current USMs are inapplicable as most of their vibrators, which are core components of USMs, are made of stainless steel or aluminum alloy. In previous studies [10–15], we bonded vibrating bodies made of poly phenylene sulfide (PPS), a functional polymer with low mechanical loss [10,11], on lead zirconate titanate (PZT) disks to form double-layered motors. They provided high rotation speeds and light weight but limited output torques and power due to the low stiffness of the polymer parts [14]. Utilization of rigid ceramics would be a possible method of enhancing the stiffness [16]. However, our recent study [17] found that the vibrator of which the entire vibrating body was made of rigid ceramics easily fractured even at a low voltage as it exhibited extremely large stress due to the high stiffness. As a consequence, this motor did have the capability to provide a good performance. To overcome these drawbacks, in this study, we develop a new vibrator with a triple-layered structure: A thin disk made of rigid ceramics is sandwiched between the PPS vibrating body and PZT disk; using this structure, the stiffness can be adjusted by changing the dimensions of each layer. To date, several triple-layered (or multi-layered) vibrators for USMs have been reported. Thin films, typically made of nitrides and oxides, were coated on metal vibrating bodies to improve the frictional and/or abrasional properties [18–20]. But these studies did not focus on the vibration characteristics. Actually, the films were too thin to affect the vibration characteristics. Recently, Li et al. have bonded metal/polymer-matrix materials on metal plates to form multi-layered vibrators [21], of which the matrix-material layers have the thicknesses comparable to the metal layers, and analyzed how the material constants and dimensions affect the frictional loss. However, how the motor properties, e.g. the elliptical motion shapes, force factors, and load characteristics, depended on the geometrical parameters were not discussed. It is necessary to systemically investigate these dependences for structural optimization.

In this study, first, we preliminarily select the suitable ceramic(s) as the middle layer by measuring the damping coefficients of

* Corresponding author.
E-mail address: wujiang@sonic.pi.titech.ac.jp (J. Wu).

https://doi.org/10.1016/j.sna.2018.09.069
0924-4247/

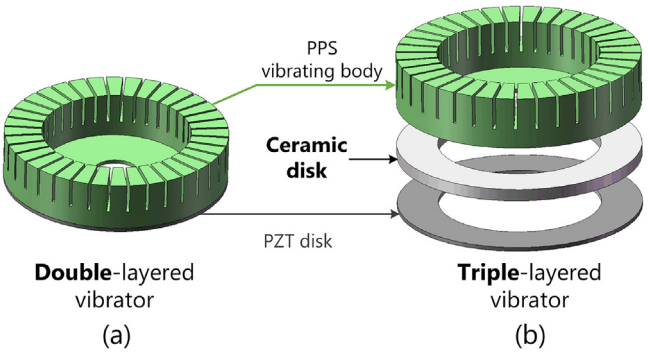

Fig. 1. Schematics of (a) PPS/PZT double-layered and (b) PPS/rigid-ceramic/PZT triple-layered vibrators.

several functional rigid ceramics. Subsequently, we analyze the elliptical motion shapes and the force factors of triple-layered vibrators as the thicknesses of the PPS vibrating bodies and the rigid ceramic layers are varied. Finally, we measure the load characteristics of the motors with triple-layered vibrators. As the first report regarding the PPS/alumina/PZT triple-layered motors, this paper focuses on the load characteristics as they are the fundamental performance for USMs [1,2]. Other performance, such as motion precision, will be explored in our further studies.

2. Triple-layered vibrator

2.1. Basic configuration

Fig. 1(a) and (b) illustrate the configurations of the double- and triple-layered vibrators, respectively. In the previous design, a PPS vibrating body with periodical slots is directly bonded on a thin PZT disk. The slotted upper surface contacts the rotor and generate frictional force. The ceramic disk is sandwiched between the PPS vibrating body and the PZT disk in the new design. The three bodies are bonded firmly with epoxy resin to achieve high reliability of this motor. Since the ceramic disk has a simple shape, there exists almost no difference in the structural complexity between the triple- and double-layered vibrators.

2.2. Selection of middle layer

To date, there have been no reports regarding the mechanical damping coefficients of rigid ceramics at several tens of kilohertz [10,11]. Thus, prior to evaluation of triple-layered vibrators, the damping coefficients were measured via the impact method to

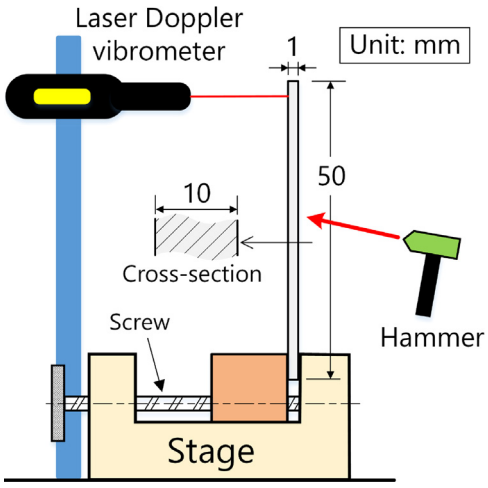

Fig. 2. Experimental setup for measuring the damping coefficients of the tested rigid ceramics.

select suitable one(s) as the middle layer [10,12]. Alumina, steatite, silicon carbide, and aluminum nitride are tested as they have wide industrial applications [16]. Their material constants are listed in Table 1. Fig. 2 schematically illustrates the experimental setup. Several rectangular plates 50 mm in length, 10 mm in width, and 1 mm in thickness were prepared, and one end of them was tightly fixed with a screw. We hammered the middle part of the plate to apply an impulse mechanical input, and measured the vibration velocities of the free end with an out-of-plane laser Doppler vibrometer (NLV1232, Polytec, Waldbronn, Germany). The vibration velocity $y(t)$ is theoretically expressed as

$$y(t) = A\exp\left(-\beta\omega t\right)\sin\left(\omega t + \vartheta\right), \quad (1)$$

where 2β, ω, A, and ϑ are the damping coefficient, angular frequency, initial amplitude, and phase, respectively. Fig. 3(a) and (b) show the damped oscillation of the alumina plate and an exponential fitting of the envelope, and the response in frequency domain, respectively. The results shown in Fig. 3 demonstrate that $\beta\omega = 11.82$ and $\omega = 42{,}454$ rad/s. Therefore, the damping coefficient 2β is 0.0005. For each sample, the damping coefficients are measured for 20 times and the average values are indicated in Fig. 4. Silicon carbide exhibits a damping coefficient of 0.0006, comparable to the value of alumina. However, the silicon carbide samples easily fractured in our experiments; this is assumed to be caused by the fragility [22]. Thus, alumina is employed as the middle layer in our trial.

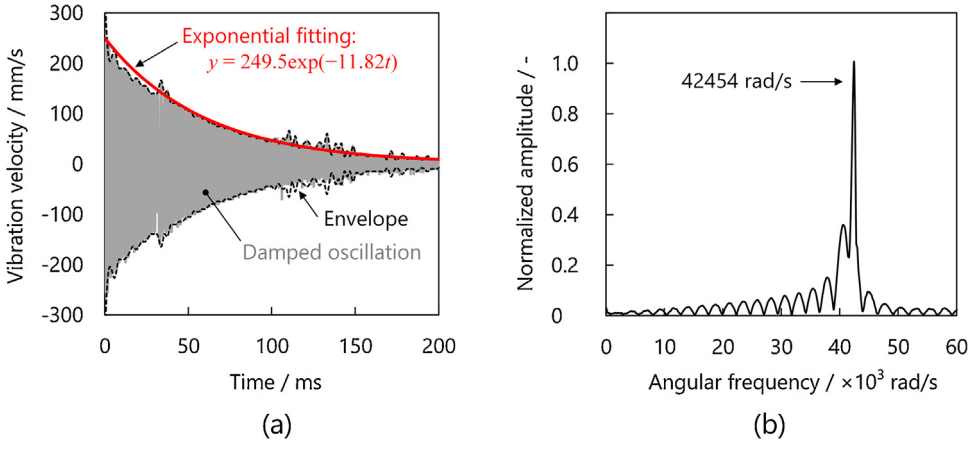

Fig. 3. (a) Damped oscillation of alumina plate under an impulse mechanical input and (b) its response in frequency domain.

Table 1
Mechanical constants of polymers and ceramics.

Materials		Density/$\times 10^3$ kg/m^3	Elastic modulus/GPa	Poisson's ratio
Polymer	PPS	1.35	3.45	0.36
Ceramics	Alumina (Al_2O_3)	3.90	390	0.23
	Steatite ($3MgO{\cdot}4SiO_2{\cdot}H_2O$)	2.80	120	0.22
	Silicon carbide (SiC)	3.10	410	0.16
	Aluminum nitride (AlN)	3.30	320	0.24

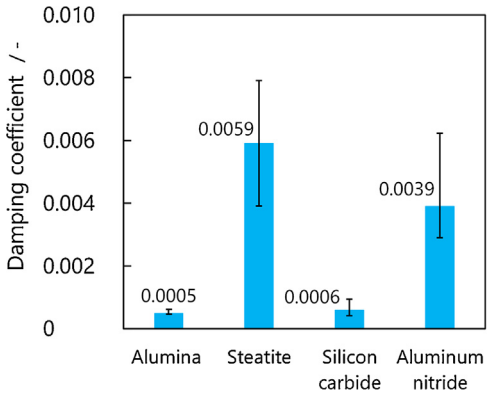

Fig. 4. Measured damping coefficients of alumina, steatite, silicon carbide, and aluminum nitride.

3. Vibration characteristics of triple-layered vibrators

3.1. Practical design of triple-layered vibrator

Fig. 5(a) detailedly illustrates the structure and dimensions of the triple-layered vibrator. The PPS vibrating body had a cylindrical part 20 and 30 mm in inner and outer diameters, respectively, and a bottom disk 0.5 mm in thickness. Radial slots 0.5 mm in width and 4 mm in depth were created on the cylindrical part with an interval of 10°. A polar coordinate (z, r, and θ axes) is established on the top surface. The PZT disk (C213, Fuji Ceramics, Fujinomiya, Japan) had inner and outer diameters of 20 and 30 mm, respectively, and a thickness of 0.5 mm. As shown in Fig. 5(b), the bottom surface of the PZT disk was evenly divided into 12 parts (I–XII). The opposite side without division was bonded to one side of the alumina annular disk, of which the inner and outer diameters were respectively identical to those of the PZT disk. The other side of the alumina disk was glued to the bottom surface of the PPS vibrating body. The ceramic disk thickness s and the un-slotted part thickness t of the PPS vibrating body are varied in this study.

3.2. Principle

When sinusoidal voltages $\sin(\omega_0 t)$, $\cos(\omega_0 t)$, $-\sin(\omega_0 t)$, and $-\cos(\omega_0 t)$, where ω_0 denotes the resonance frequency, are applied to the electrodes I, V, and IX; II, VI, and X; III, VII, and XI; and IV, VIII, and XII; respectively, as shown in Fig. 5(b), two standing waves in the 3rd bending modes:

$$u_1(t,\theta) = U\sin(\omega_0 t)\sin(k\theta) \tag{2}$$

and

$$u_2(t,\theta) = U\cos(\omega_0 t)\cos(k\theta) \tag{3}$$

are excited. Here, θ, U, and k denote the circumferential angle, vibration amplitude, and wave number ($k=3$), respectively. A traveling wave is formed by the superposition of these standing waves:

$$u_z(t,\theta) = \sum_{i=1}^{2} u_i(t,\theta) = U\cos(\omega_0 t - k\theta). \tag{4}$$

In flexural vibration, the θ-axis vibration velocity is derived from u_z:

$$u_\theta(t,\theta) = -\varsigma\cdot\frac{\partial u_z(t,\theta)}{\partial\theta} = \varsigma kU\sin(\omega_0 t - k\theta), \tag{5}$$

where ς is a ratio determined by the vibrator structure and the vibration mode. Thus,

$$\left[\frac{u_z(t,\theta)}{U}\right]^2 + \left[\frac{u_\theta(t,\theta)}{\varsigma kU}\right]^2 = 1. \tag{6}$$

The elliptical motion drives the rotor pressed to its upper surface via frictional force. Along the r axis, there also exist vibration components, which have 180° phase differences with those along the z axis. Thus, the trajectories in the z-r planes are lines. The elliptical motion shapes, indicated by the ratios v_θ/v_z ($=\varsigma k$) and v_r/v_z, greatly affect the motor performance [1,2,14,15]. Here, v_z and v_r are respectively the vertical and radial vibration velocities at antinodes, and v_θ is the circumferential vibration velocity at nodes. The

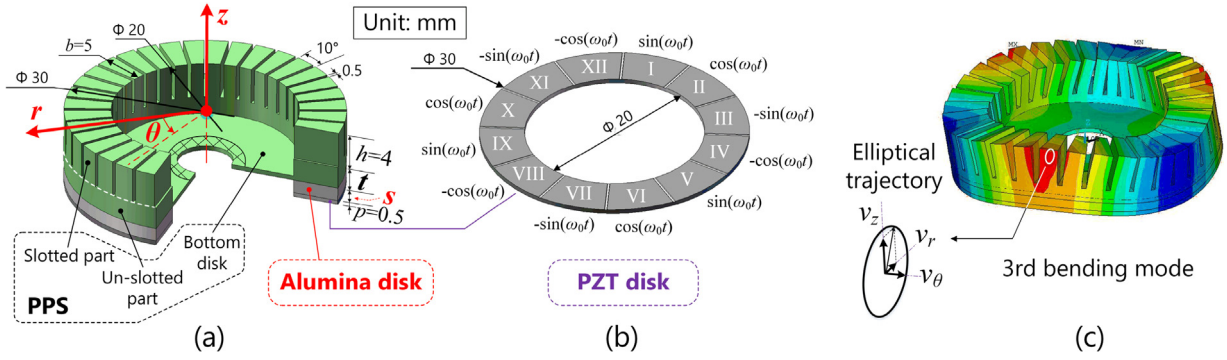

Fig. 5. Triple-layered vibrator. (a) Configuration and dimensions, where h, t, s, p, and b represent the height of the slotted part (4 mm), the thickness of the un-slotted part of the PPS vibrating body, the thickness of the alumina disk, the thickness of the PZT disk (0.5 mm), and the radial thickness (5 mm), respectively. (b) the PZT disk and the voltage applied to each electrode. (c) The 3rd bending vibration mode.

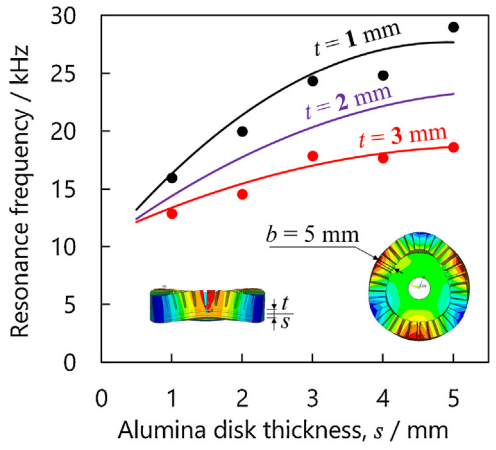

Fig. 6. Resonance frequencies of the 3rd order bending mode as functions of the thicknesses of alumina disk and un-slotted PPS part. The curves and dots are simulated and experimental results, respectively.

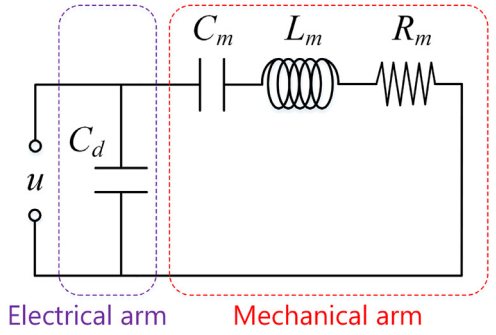

Fig. 7. Equivalent circuit model.

other essential indicator is the force factor, defined as the ratio of the current i to the circumferential vibration velocity v_θ [23].

3.3. Vibration characteristics

First, through finite element analysis [software: ANSYS (ver. 16.0, ANSYS Inc., Canonsburg, USA)], we investigated the resonance frequencies f_r of triple-layered vibrators when the alumina disks and the un-slotted parts of PPS vibrating bodies had different thicknesses. As illustrated in Fig. 6, in the cases of the vibrators with 1-mm-thick un-slotted parts, the resonance frequencies increased from 16 to 25 kHz as the ceramic disk thicknesses increased from 1 to 3 mm because of the increased bending stiffness. When the alumina disk was sufficiently thick (>3 mm), the vibrators dominantly exhibited bending vibrations along the r axis instead of the z axis, and the resonance frequencies approached the saturated values because they were dominantly determined by the radial thicknesses b of the PPS un-slotted parts [14]. Besides, the vibrators with identical alumina disk thicknesses showed lower resonance frequencies when the PPS vibrating bodies had thicker un-slotted parts. However, the double-layered vibrators exhibit increases in resonance frequencies as they become thicker [14,24]. Here, a simplified equivalent circuit model [1,23] is introduced to explain the reason.

As illustrated in Fig. 7, an electrical and a mechanical arm are parallelly connected in this model [1,6]. The electrical arm contains the clamped capacitance C_d, whereas the mechanical arm consists of three serially connected elements, i.e. the equivalent stiffness $1/C_m$, mass L_m, and damper R_m; these parameters can be calculated from admittance characteristics [measured with an impedance analyzer (4294 A, Agilent, Santa Clara, CA, USA)] using the following equations:

$$\frac{1}{C_m} = \frac{2\pi f_0 \cdot Q}{Y_{m0}}, \tag{7}$$

$$L_m = \frac{Q}{2\pi f_0 \cdot Y_{m0}}, \tag{8}$$

and

$$R_m = \frac{1}{Y_{m0}}. \tag{9}$$

Here, f_0 represents the resonance frequency, Q denotes the mechanical quality factor (Q=$f_0/\Delta f_r$, where Δf_r represents the bandwidth corresponding to 0.707 times of the maximal vibration amplitude), and Y_{m0} is the motional admittance. The clamped capacitance equals $\Delta Y_{nr}/\Delta\omega_{nr}$, where ΔY_{nr} and $\Delta\omega_{nr}$ represent the variations in admittance and angular frequency, respectively, in the non-resonant portion of an admittance curve. Table 2 lists the equivalent circuit parameters of the vibrators with s = 1 mm and t = 1 mm (s1t1) as well as s = 1 mm and t = 3 mm (s1t3). The equivalent mass of the s1t3 vibrator is 4 times the value of the s1t1 vibrator because the s1t3 vibrator is thicker. Whereas the equivalent stiffness is twice higher for the s1t3 vibrator than for the s1t1 vibrator. Since the density difference is not large between alumina and PPS, and in the meantime, the un-slotted parts of the PPS vibrating bodies have the thicknesses comparable to the alumina disks, the equivalent mass dominantly depends on their thicknesses. The variation in the equivalent stiffness should be smaller than the change in the equivalent mass because the difference in the elastic moduli between alumina and PPS is larger than that in the densities. In contrast, the double-layered vibrators have increasing resonance frequencies dominantly because their stiffness becomes higher with increasing thickness [14].

Subsequently, we discussed how the elliptical motion shape and the force factor depend on the thicknesses of each layer. Fig. 8(a) demonstrates that the ratios v_θ/v_z have negligibly small variations, while the ratios v_r/v_z exhibit observable variations as the alumina disks became thicker. For instance, the ratios v_r/v_z of the vibrators with 1-mm-thick PPS un-slotted parts increased gradually in the ranges of 0.5–2.0 mm and 3.5–5.0 mm. However, it sharply increased from 1.0 to 2.5 when the alumina disk thicknesses increased from 2.0 to 3.5 mm. It is assumed to originate from the aforementioned change in the dominant vibration modes. Fig. 8(b) illustrates the variations in force factors against the alumina disk thickness. The vibrators with 1-, 2-, and 3-mm-thick un-slotted parts provided the maximal force factors when the alumina disks had the thicknesses of 0.8, 1.7, and 2.2 mm, respectively. Whereas the force factors of the double-layered vibrators with practical thicknesses (<10 mm) exhibited monotonous enhancements with increasing thickness [14]. This difference can be explained on the basis of the positions of neutral axes on the cross-sections of vibrators.

3.4. Neutral axis

Fig. 9(a) shows a simplified model for calculating the neutral position. The θ-axis vibration velocity equals zero at the neutral position, and increases proportionally to the distance from the neutral position [24]. The neutral axis locates (i) in the PZT disk, (ii) at the boundary between the PZT and alumina disks, and (iii) in the alumina disk when the vibrators have thick, moderate, and thin alumina disks, respectively. In the cases (i) and (iii), the neutral positions z_N can be respectively obtained by solving the following equations [24]:

Table 2
Equivalent circuit parameters of s1t1 and s1t3 vibrators.

Vibrator	Clamped capacitance, $C_d/\times10^{-12}$ F	Equivalent mass, L_m /H	Equivalent stiffness, $1/C_m/\times10^{12}$ F^{-1}	Equivalent damper, $R_m/\times10^{3}$ Ω
s1t1	6.94	43.8	0.435	15.0
s1t3	6.89	158.1	0.974	38.7

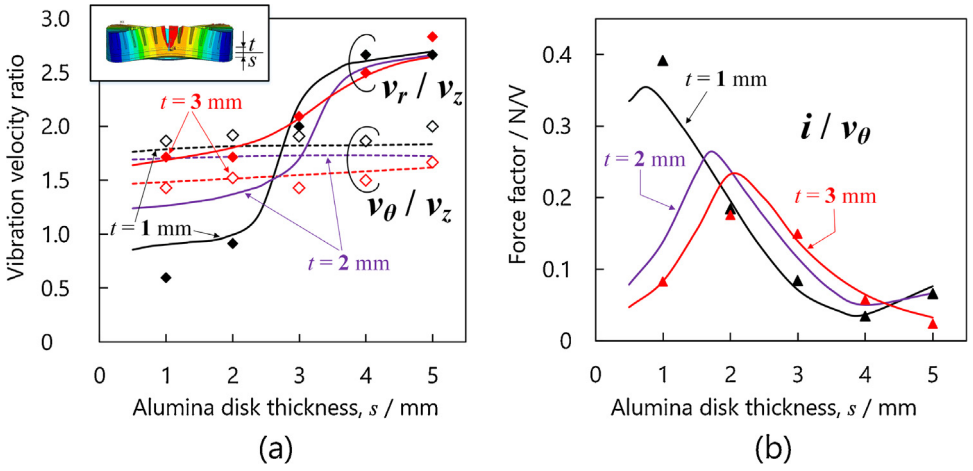

Fig. 8. (a) Ratios v_θ/v_z and v_r/v_z and (b) force factors of the vibrators with different thicknesses of alumina disks and un-slotted PPS parts. The curves and dots are simulated and experimental results, respectively.

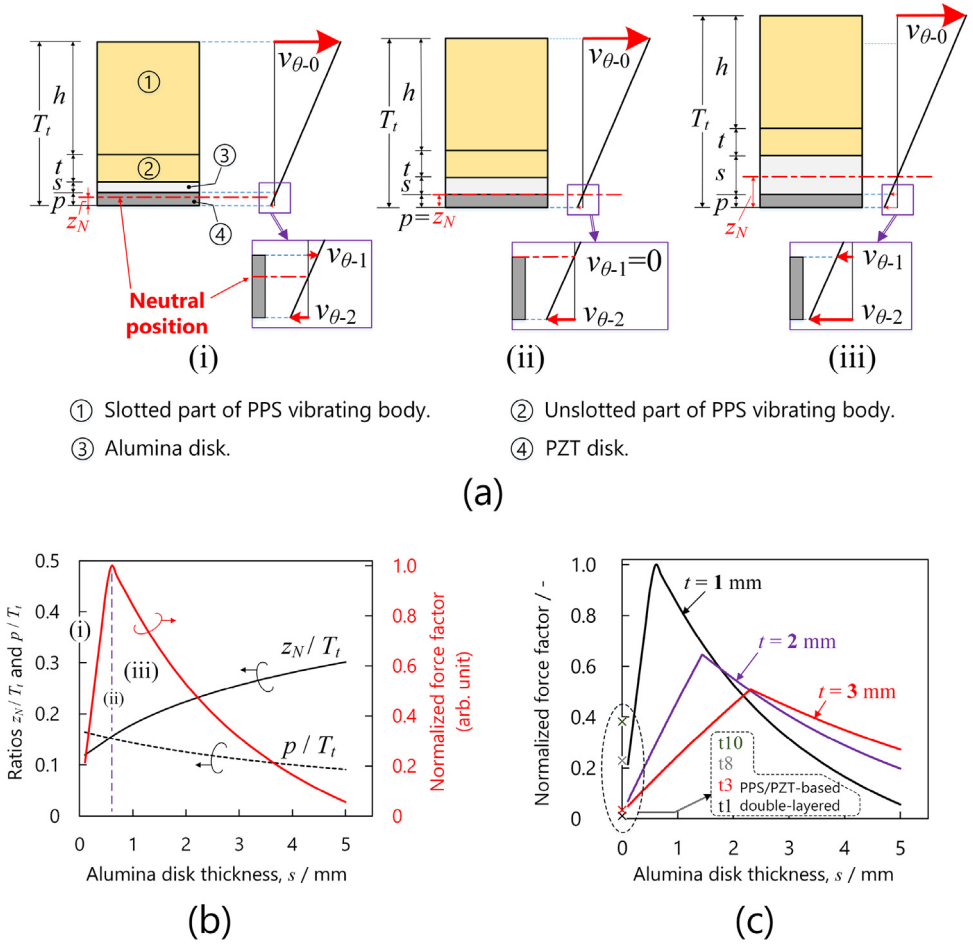

Fig. 9. (a) Neutral positions on the vibrators with (i) thin, (ii) moderate, and (iii) thick alumina disks. (b) Ratios z_N/T_t and p/T_t, and force factors of the vibrators with 1-mm-thick un-slotted parts. (c) Force factors of the triple-layered vibrators. Here, t1, t3, t8, and t10 represent the PPS/PZT double-layered vibrators with 1-, 3-, 8-, and 10-mm-thick un-slotted parts, respectively.

$$E_{PPS}\int_{p-z_N+s}^{p-z_N+s+t+h} zdS + E_{Alu}\int_{p-z_N}^{p-z_N+s} zdS + E_{PCE}\int_{0}^{p-z_N} zdS + E_{PCE}\int_{-z_N}^{0} zdS = 0 \quad (10)$$

and

$$E_{PPS}\int_{s+p-z_N}^{s+p-z_N+t+h} zdS + E_{Alu}\int_{0}^{s+p-z_N} zdS + E_{Alu}\int_{p-z_N}^{0} zdS + E_{PCE}\int_{-z_N}^{p-z_N} zdS = 0, \quad (11)$$

where E_{PPS}, E_{Alu}, and E_{PCE} denote the elastic moduli of PPS, alumina, and PZT (c_{11} = 131 GPa), respectively, and dS represents an elementary area (=$b{\cdot}dz$). The force factor can be estimated as [25]

$$A_f = \frac{e_{31}S_e}{p}\cdot\left|\frac{v_{\theta-1}-v_{\theta-2}}{v_{\theta-0}}\right| = \begin{cases} \dfrac{e_{31}S_e}{p}\cdot\left|\dfrac{2z_N-p}{T_t-z_N}\right| & \text{when } z_N \le p \\ \dfrac{e_{31}S_e}{p}\cdot\left|\dfrac{p}{T_t-z_N}\right| & \text{when } z_N > p \end{cases}, \quad (12)$$

where $v_{\theta\text{-}0}$, $v_{\theta\text{-}1}$, and $v_{\theta\text{-}2}$ are respectively the θ-axis vibration velocities at the upper surface of the PPS vibrating body, and the upper and bottom surfaces of the PZT disk; T_t is the total thickness (=h+t+s+p); S_e is the electrode area; and e_{31} is the piezoelectric coefficient.

Fig. 9(b) plots the ratios z_N/T_t and p/T_t, and the force factor as functions of the alumina disk thickness when the PPS vibrating body has a 1-mm-thick un-slotted part. When the neutral position locates on the PZT disk, its position advances upwards along the z axis. The force factor becomes higher because the alumina disk exhibits higher stiffness. It reaches the maximal value when the neutral axis is close to the boundary between the PZT and alumina disks. Fig. 9(c) illustrates the force factors of other triple-layered vibrators. Clearly, they have almost the same tendencies with the results shown in Fig. 8(b); this validates the effectiveness of this model. The PPS/PZT double-layered vibrators exhibit their neutral axes in PZT disks [similar to the case (a) for triple-layered ones] owing to the relatively high elastic moduli of PZT compared to polymers. Their force factors increase as the PPS vibrating bodies become thicker. It is predictable that double-layered vibrators provide their maximal force factor when their PPS vibrating bodies have sufficient thicknesses. But in the meantime, there exist high vibration components in the radial directions, leading to high frictional loss on the contact surfaces and consequently low performance of motors [14]. Fig. 9(c) also demonstrates that, for the double-layered vibrators applicable to USM (<10 mm), the force factors are lower than the values of the triple-layered vibrators.

4. Motor performance

4.1. Experimental setup

Using the transient method [26], we measured the load characteristics of motors with varying geometrical shapes. Fig. 10(a)

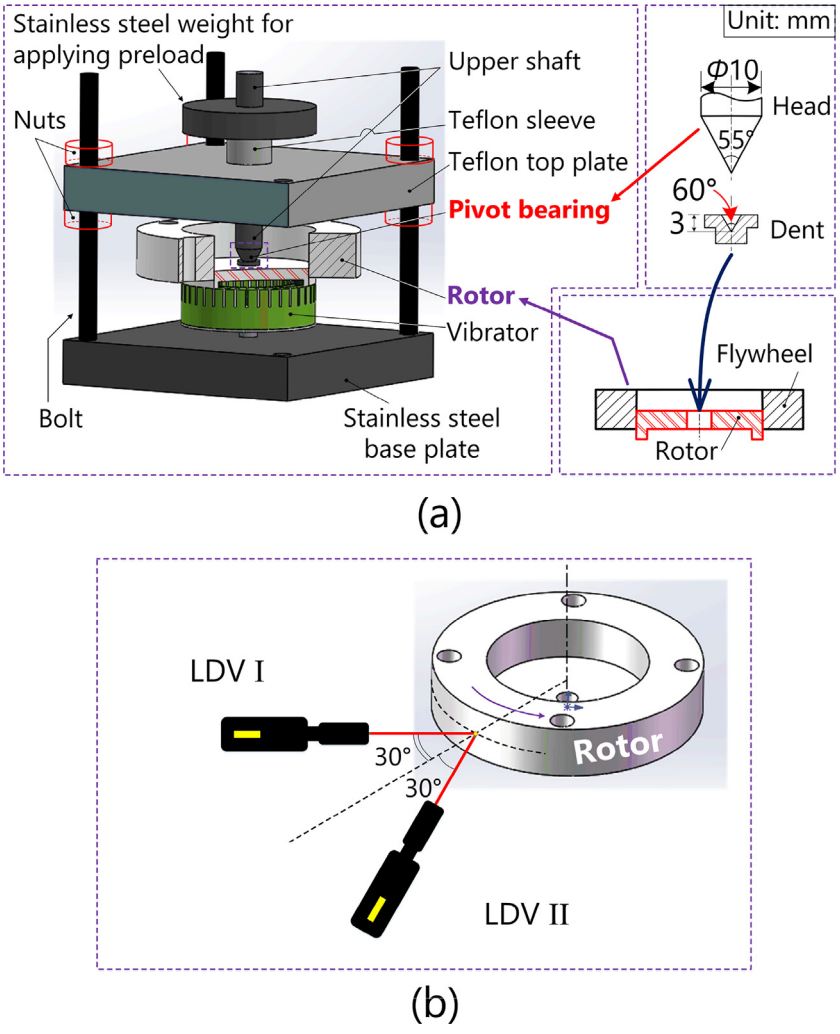

Fig. 10. (a) Testbed for evaluating motor performance and (b) method of measuring rotation speeds [14,15].

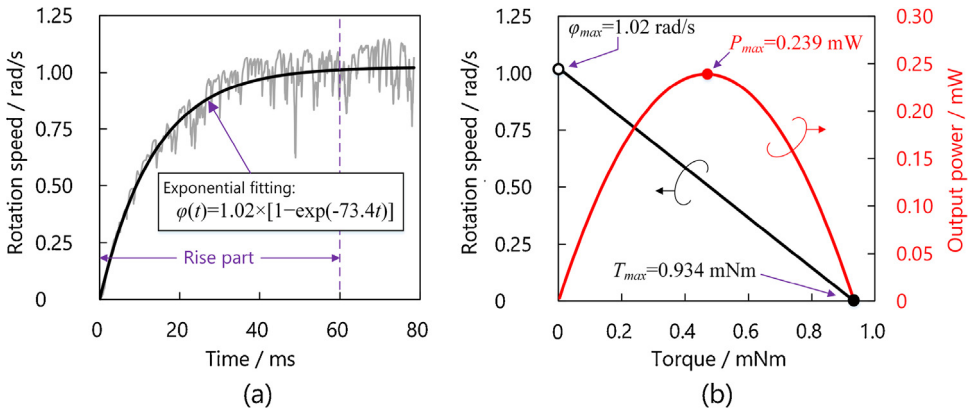

Fig. 11. (a) Transient response (grey curve) of rotation speed and its exponential fitting curve (black curve). (b) Load characteristics of the s1t3 motor at 65 V (For interpretation of the references to colour in this figure legend, the reader is referred to the web version of this article).

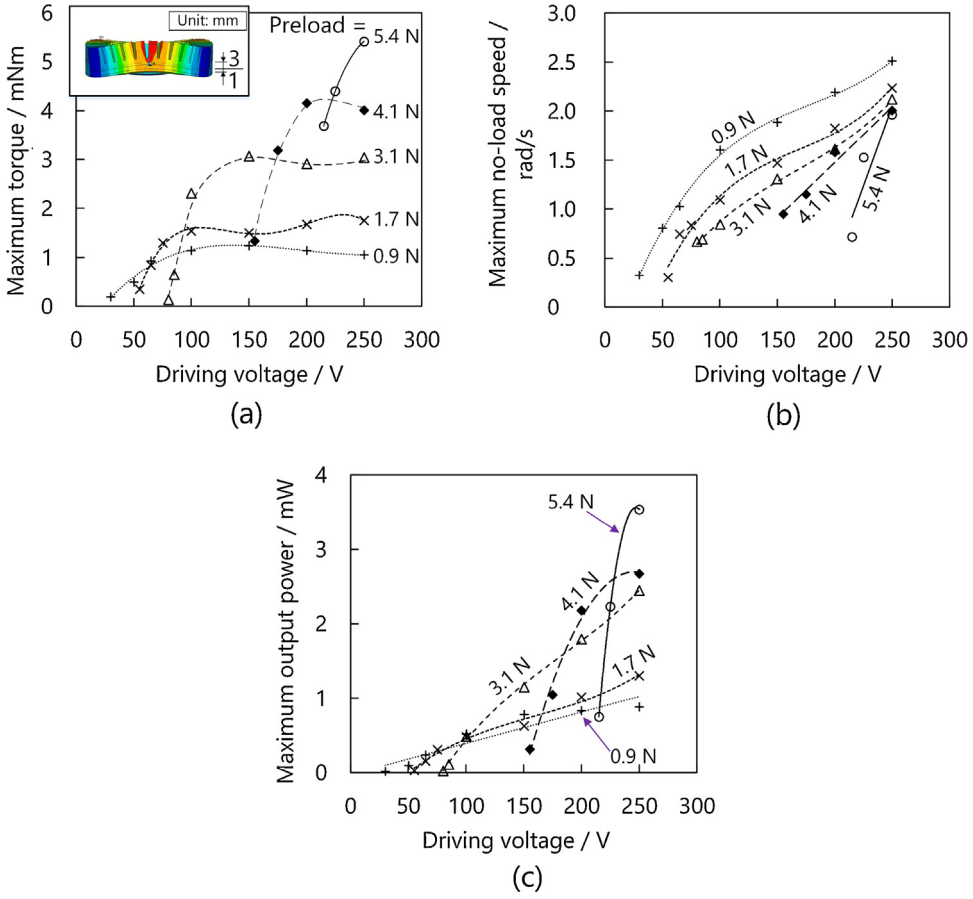

Fig. 12. Performance of the s1t3 motor as functions of driving voltages under different preloads: (a) Maximum torque, (b) maximum no-load angular velocity, and (c) maximum output power.

depicts the testbed repeatedly used in our previous studies [14,15]: The vibrator was clamped to a shaft fixed to a stainless-steel base plate. A pivot bearing composed of a conical head and a dent, of which the cone angles were respectively 55° and 60°, was employed to lower the frictional loss. The upper shaft of the bearing was inserted into a sleeve made of Teflon, and the dent was fixed at the center of the rotor. The preload was adjusted by changing the weights applied to the shaft. The transient responses of rotation speeds were measured with two laser Doppler vibrometers: As shown in Fig. 10(b), two beams illuminated the same point on the outer surface of the rotor with the same angles. The rotation speed was obtained from the outputs of these two vibrometers based on a simple geometry [27].

4.2. Case study

Fig. 11(a) showed the transient response of the s1t3 motor when a voltage of 65 V and a preload of 0.9 N were applied. The rotation speed initially exhibited a rapid increase, and at 60 ms, it approached the saturated value of 1.02 rad/s. Since the transient response included high-frequency fluctuations caused by the ultrasonic vibration components, it was fitted with an exponential function:

$$\varphi(t) = \varphi_{max} \cdot [1 - \exp(-\alpha t)], \tag{13}$$

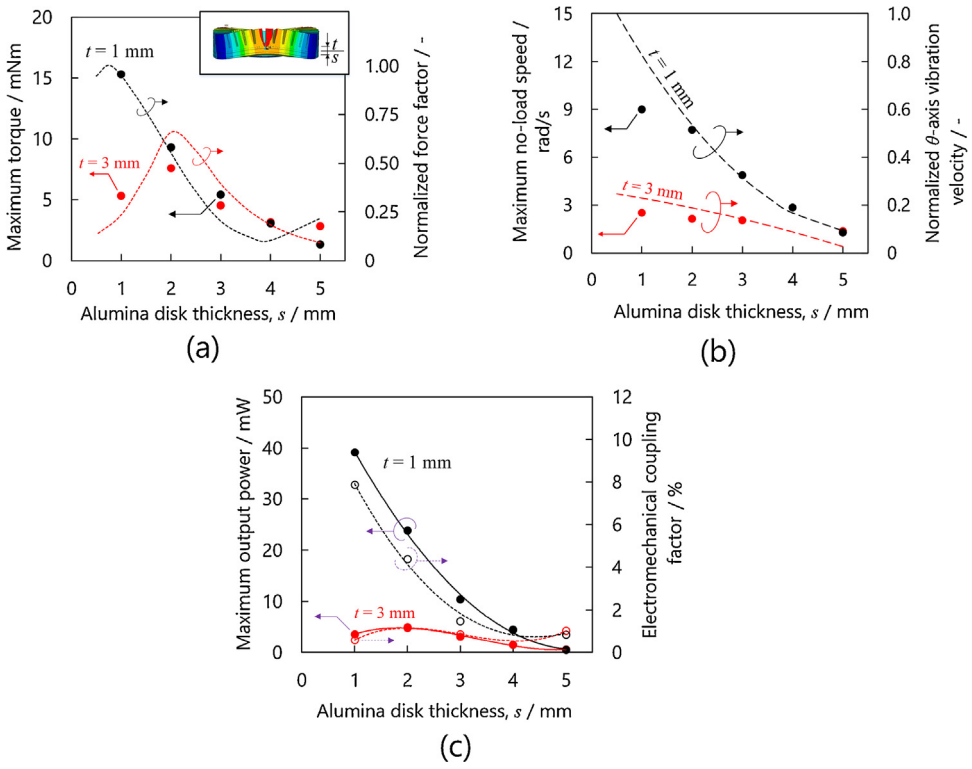

Fig. 13. (a) Maximum torques, (b) maximum no-load rotation speeds, and (c) maximum output powers of the motors with different thicknesses of alumina disks and un-slotted PPS parts at 250 V and electromechanical coupling factors of the vibrators. The curves in (a) and (b) xare simulated results, while those in (c) are fitting curves.

where φ_{max} and $1/\alpha$ represent the saturated rotation speed and rise time, respectively [25]. The instantaneous output torque and power are expressed as

$$T(t) = J \cdot \frac{d[\varphi(t)]}{dt} \tag{14}$$

and

$$P(t) = J \cdot \frac{d[\varphi(t)]}{dt} \cdot \varphi(t), \tag{15}$$

respectively, where J denotes the moment of inertia of the flywheel and equals 1.24×10^{-5} kg m^2. By deleting the time, the rotation speed and output power are presented versus the torque. Fig. 11(b) plots the results. The motor yielded its maximum torque of 0.934 mN m when the rotor started to rotate. At a moderate torque, the motor yielded the maximum output power of 0.239 mW.

Fig. 12(a)–(c) respectively demonstrate the maximum torque, no-load rotation speed, and output power of the s1t3 motor as functions of the driving voltage at different preloads. Dead regions in the torque and no-load speed existed when a low voltage was applied. Initially, the output torque increased proportionally to the voltage, and saturated at a high voltage because it was limited by the frictional force [25]. The rotation speed increased as the voltage became higher. The maximum output power of 3.4 mW was obtained at 250 V with the preload of 5.4 N.

4.3. Load characteristics of motors with varying dimensions

Fig. 13 shows the load characteristics of tested motors as functions of the thicknesses of their alumina disks and the PPS un-slotted parts. The applied voltages were set to 250 V. As plotted in Fig. 13(a), the maximum torques of the motors with the 1-mm-thick PPS un-slotted parts monotonously decreased from 15 to 2 mN·m as the thickness of alumina disk increased from 1 to 5 mm. However, among the motors with the 3-mm-thick PPS un-slotted parts, the one with the 2-mm-thick alumina disk yielded a relatively high torque. Clearly, the variations in the maximum torques originates from the changes in the force factors [2,14,28]. Fig. 13(b) illustrates that, because the θ-axis vibration velocity decreases as the alumina disk becomes thicker, there exists a reduction in the maximum no-load rotation speed [1,2]. As shown in Fig. 13(c), the electromechanical coupling factor becomes lower with increasing thickness, and leads to the reduction in output power [29]. It is worth mentioning that the s5t1 and s5t3 motors have lower output powers than the s4t1 and s4t3 ones though they have higher electromechanical coupling factors because the negative effects caused by undesirable vibration components offset the positive effects caused by the enhancements in the electromechanical coupling factors [14]. Besides, in the cases of the s5t1 and s5t3 vibrators, bending vibration are dominantly excited on the slotted parts of PPS vibrating bodies rather than the un-slotted parts and alumina disks because the slotted parts have lower bending stiffness [15]; this is assumed to result in the relatively high electromechanical coupling factors of the s5t1 and s5t3 motors compared to those of the s4t1 and s4t3 motors.

Table 3 compares the performance of motors with PPS/alumina/PZT triple-layered vibrators with those with PPS/PZT double-layered vibrators [14]. The maximum torque of the s1t1 motor is 5 times higher than the value of the PPS/PZT motor owing to not only the enhancement in force factors but also the reduction in undesirable vibration components (represented by v_r/v_z). More importantly, the maximal thickness is lower for the triple-layered than the double-layered vibrators. The s1t1 motor yields a maximum output power of 39.4 mW, which exceeds 13 times the value of the PPS/PZT motor. Since alumina has lower damper coefficients than polymers, the triple-layered vibrator provides lower mechanical loss (represented as the equivalent damper), which possibly leads to a higher efficiency for the s1t1

Table 3
Comparison in performance of USMs with PPS/alumina/PZT triple-layered and PPS/PZT double-layered vibrators.

Performance	USM with triple-layered vibrator	USM with double-layered vibrator
Maximum output torque at 250 V/mNm	15.2	2.9
Optimal thickness corresponding to maximum output torque/mm	2 (s = 1 mm, t = 1 mm)	8
Force factor/N·V^{-1}	0.4	0.1
Ratio v_r/v_z	0.9	2.5
Maximum no-load rotation speed at 250 V/rad s^{-1}	8.9	16.1
Optimal thickness corresponding to maximum no-load rotation speed/mm	2	2
Maximum output power at 250 V/mW	39.1	3.0
Optimal thickness corresponding to maximum output power/mm	2	2
Electromechanical coupling factor/%	7.9	0.4
Maximum efficiency/%	8.3	4.8
Equivalent damper/$\times 10^3$ Ω	15.0	45.0
Maximum power density/W kg^{-1}	10.3	2.5

motor than for the double-layered motor. Besides, the weight of the triple-layered motor slightly increases compared to the double-layered one owing to the moderate density of alumina and low thickness of the disk; this causes a higher power density of the PPS/alumina/PZT triple-layered motor.

5. Conclusions

In this study, we developed a PPS/alumina/PZT triple-layered vibrator as a core component of USM. After discussing the vibration characteristics of vibrators and measuring the load characteristics of motors, we have drawn the following conclusions:

(1) The PPS/alumina/PZT triple-layered vibrator exhibited the maximum force factor when its neutral axis was close to the boundary between the PZT and alumina disks.
(2) Relatively high output torque and power were obtained on the triple-layered motor with the smallest thickness.
(3) The triple-layered motor exhibited the maximum output torque and power of 15.2 mN m and 39.3 mW, respectively 5 and 13 times the values achieved on our previously reported double-layered motors.

We have gained an understanding on the triple-layered motors and anticipate that the obtained results will provide adequate information for further optimization. To achieve the practical applications in chemical industry, the accessory components of motors, e.g. feeding lines and bearings, will be carefully selected or specially designed in the future.

Acknowledgement

The authors thank the staffs with the Precision and Manufacturing Center, Technical Department, Tokyo Institute of Technology, for machining the motor components. This work was supported by the Japan Society for the Promotion of Science (JSPS) KAKENHI Grant Number 17J05057. JSPS KAKENHI Grant Number 17J05057.

References

[1] S. Ueha, Y. Tomikawa, M.K. Kurosawa, K. Nakamura, Ultrasonic Motors—Theory and Applications, New York, USA, 1993.
[2] K. Nakamura, M. Kurosawa, S. Ueha, Characteristics of a hybrid transducer-type ultrasonic motor, IEEE Trans. Ultrason. Ferroelectr. Freq. Control 38 (1991) 188–193.
[3] Z. Zhu, S. To, K.F. Ehmann, X. Zhou, Design, analysis, and realization of a novel piezoelectrically rotary spatial vibration system for micro-/nanomachining, IEEE ASME Trans. Mechatron. 22 (2017) 1227–1237.
[4] L. Yan, D. Liu, H. Lan, Z. Jiao, Compact traveling wave micro motor based on shear electromechanical coupling, IEEE ASME Trans. Mechatron. 21 (2016) 1572–1580.
[5] X. Zhou, Y. Zhang, Q. Zhang, A novel linear ultrasonic motor with characteristic of variable mode excitation, Ceram. Int. 43 (2017) S64–S69.
[6] K. Nakamura, Ultrasonic Transducers, Woodhead Publishing Limited, Cambridge, UK, 2012.
[7] Q. Zhang, S. Shi, W. Chen, An electromechancial coupling model of a longitudinal vibration type piezoelectric ultrasonic transducer, Ceram. Int. 41 (2015) S638–S644.
[8] L. Zheng, S. Liu, S. Wang, Current situation and future of Chinese industrial robot development, Int. J. Mech. Eng. Rob. Res. 5 (2016) 295–300.
[9] H. Nishioka, A. Takeuchi, The Development of High Technology Industry in Japan, in: The Development of High Technology Industries—An International Survey, 1st ed., Routledge, Taylor & Francis Group, New York, USA, 2018.
[10] J. Wu, Y. Mizuno, M. Tabaru, K. Nakamura, Measurement of mechanical quality factors of polymers in flexural vibration for high-power ultrasonic application, Ultrasonics 69 (2016) 74–82.
[11] J. Wu, Y. Mizuno, K. Nakamura, Enhancement in mechanical quality factors of poly phenylene sulfide under high-amplitude ultrasonic vibration through thermal annealing, Ultrasonics 91 (2019) 52–61.
[12] J. Wu, Y. Mizuno, M. Tabaru, K. Nakamura, Ultrasonic motors with polymer-based vibrators, IEEE Trans. Ultrason. Ferroelectr. Freq. Control 62 (2015) 2169–2177.
[13] J. Wu, Y. Mizuno, K. Nakamura, Vibration characteristics of polymer-based Langevin transducers, Smart Mater. Struct. 27 (2018), 095013.
[14] J. Wu, Y. Mizuno, K. Nakamura, Structural parameter study on polymer-based ultrasonic motor, Smart Mater. Struct. 26 (2017), 115022.
[15] J. Wu, Y. Mizuno, K. Nakamura, Polymer-based ultrasonic motor utilizing high-order vibration modes, IEEE Trans. Mechatron. 23 (2018) 788–799.
[16] D. Sherman, D. Brandon, Mechanical properties and their relation to microstructure, in: Handbook of Ceramic Hard Materials, Wiley-VCH Press, Weinheim, Germany, 2000.
[17] J. Wu, Y. Mizuno, and K. Nakamura, Trail fabrication of traveling wave ultrasonic motor with alumina-based vibrator, Symposium on Ultrasonic Electronics (2018), 1J1-5.
[18] J. Qu, Y. Zhang, X. Tian, J. Li, Wear behavior of filled polymers for ultrasonic motor in vacuum environments, Wear 322 (323) (2015) 108–116.
[19] H.-P. Ko, S. Kim, J.-S. Kim, H.-J. Kim, S.-J. Kim, Wear and dynamic properties of piezoelectric ultrasonic motor with frictional materials coated stator, Mater. Chem. Phys. 90 (2005) 391–395.
[20] J. Wallaschek, Contact mechanics of piezoelectric ultrasonic motors, Smart Mater. Struct. 7 (1998) 369–381.
[21] J. Li, S. Liu, N. Zhou, A. Yu, Y. Cui, P. Chen, A traveling wave ultrasonic motor with a metal/polymer-matrix material compound stator, Smart Mater. Struct. 27 (2018), 015027.
[22] Introductions of silicon carbide and alumina productions. [Online] Available: http://www.rundum.co.jp/e/product/index6.html [Accessed: 31 June, 2018].
[23] B.F. Ley, S.G. Lutz, C.F. Rehberg, Linear Circuit Analysis, McGraw-Hill Inc., New York, USA, 1959.
[24] S.P. Timoshenko, Stresses in Transversally Loaded Beams, in Strength of Materials: Part I Elementary Theory and Problems (2nd Ver.), D. Van Nostrand Company, New York, USA, 1940.
[25] E. Mori, Vibration systems for ultrasonic applications III: parameters of equivalent electrical circuit for representing piezoelectric transducers, Ultrason. Technol. 08 (09) (1996) 59–63, In Japanese.
[26] K. Nakamura, M. Kurosawa, H. Kurebayashi, S. Ueha, An estimation of load characteristics of an ultrasonic motor by measuring transient responses, IEEE Trans. Ultrason. Ferroelectr. Freq. Control 38 (1991) 481–485.
[27] T. Shigematsu, M.K. Kurosawa, Friction drive of an SAW motor. Part I: measurements, IEEE Trans. Ultrason. Ferroelectr. Freq. Control 55 (2005) 2205–2215.
[28] X. Lu, J. Hu, C. Zhao, Analyses of the temperature field of traveling-wave rotary ultrasonic motors, IEEE Trans. Ultrason. Ferroelectr. Freq. Control 58 (2011) 2708–2719.
[29] Y. Liu, W. Chen, J. Liu, X. Yang, A high-power linear ultrasonic motor using bending vibration transducer, IEEE Trans. Ind. Electron. 60 (2013) 5160–5166.

Biographies

Jiang Wu was born in Liaoning, China, on January 29, 1988. He received the B.E. degree in mechanical engineering from Dalian University of Technology, China, in 2010. From 2010 to 2012, he studied in the State Key Laboratory of Robotics and System, Harbin Institute of Technology (HIT), China, and received the M.E. degree in mechatronic engineering from HIT in 2012. From 2012 to 2017, he studied in the Future Interdisciplinary Research of Science and Technology, Tokyo Institute of Technology (TITECH), Japan, and received Dr.Eng. degree in electrical and electronic engineering from TITECH in 2017. His research interest includes piezoresistive and piezoelectric materials, permanent-magnet-based sensing technology, and polymer-based ultrasonic transducers and actuators.

Yosuke Mizuno received the B.E., M.E., and Dr.Eng. degrees in electronic engineering from the University of Tokyo, Japan, in 2005, 2007, and 2010, respectively. From 2007 to 2010, he was involved in Brillouin optical correlation-domain reflectometry for his Dr.Eng. degree at the University of Tokyo. From 2007 to 2010, he was a Research Fellow (DC1) of the Japan Society for the Promotion of Science (JSPS). From 2010 to 2012, as a Research Fellow (PD) of JSPS, he worked on polymer optics at Tokyo Institute of Technology, Japan. In 2011, he stayed at BAM Federal Institute for Materials Research and Testing, Germany, as a Visiting Research Associate. Since 2012, he has been an Assistant Professor in the Precision and Intelligence Laboratory (presently, Institute of Innovative Research), Tokyo Institute of Technology, where he is active in fiber-optic sensing, polymer optics, and ultrasonics. Dr. Mizuno is the winner of the Ando Incentive Prize for the Study of Electronics 2011, the Konica Minolta Imaging Science Award 2014, the Japanese Society of Applied Physics (JSAP) Young Scientist Presentation Award 2015, and the Optical Society of Japan (OSJ) Optics Paper Award 2017, the Optical Design Award 2018. He is a Senior Member of the IEEE Photonics Society and a member of the JSAP, the OSJ, and the Institute of Electronics, Information, and Communication Engineers of Japan.

Kentaro Nakamura was born in Tokyo, Japan, on July 3, 1963. He received the B.E., M.E., and Dr.Eng. degrees from Tokyo Institute of Technology, Japan, in 1987, 1989, and 1992, respectively. Since 2010, he has been a Professor at the Precision and Intelligence Laboratory (presently, Institute of Innovative Research), Tokyo Institute of Technology. His research field is the applications of ultrasonic waves, measurement of vibration and sound using optical methods, and fiber-optic sensing. Prof. Nakamura is the winner of the Awaya Kiyoshi Award for Encouragement of Research from the Acoustical Society of Japan (ASJ) in 1996, and the Best Paper Awards from the Institute of Electronics, Information and Communication Engineers (IEICE) of Japan in 1998 and from the Symposium on Ultrasonic Electronics in 2007 and 2011. He also received the Japanese Journal of Applied Physics Editorial Contribution Award from the Japan Society of Applied Physics (JSAP) in 2007 and the Optical Design Award 2018. He is a member of the IEEE, the ASJ, the JSAP, the IEICE, and the Institute of Electrical Engineers of Japan. He served as the president of ASJ from 2015 to 2017.